PAPER

Check for updates

A network model of transient polymers: exploring the micromechanics of nonlinear viscoelasticity†

Robert J. Wagner, [iD] Ethan Hobbs and Franck J. Vernerey [iD] *

Dynamic networks contain crosslinks that re-associate after disconnecting, imparting them with viscoelastic properties. While continuum approaches have been developed to analyze their mechanical response, these approaches can only describe their evolution in an average sense, omitting local, stochastic mechanisms that are critical to damage initiation or strain localization. To address these limitations, we introduce a discrete numerical model that mesoscopically coarse-grains the individual constituents of a dynamic network to predict its mechanical and topological evolution. Each constituent consists of a set of flexible chains that are permanently cross-linked at one end and contain reversible binding sites at their free ends. We incorporate nonlinear force−extension of individual chains *via* a Langevin model, slip-bond dissociation through Eyring's model, and spatiotemporally-dependent bond attachment based on scaling theory. Applying incompressible, uniaxial tension to representative volume elements at a range of constant strain rates and network connectivities, we then compare the mechanical response of these networks to that predicted by the transient network theory. Ultimately, we find that the idealized continuum approach remains suitable for networks with high chain concentrations when deformed at low strain rates, yet the mesoscale model proves necessary for the exploration of localized stochastic events, such as variability of the bond kinetics, or the nucleation of micro-cavities that likely conceive damage and fracture.

1 Introduction

Dynamic networks, defined by arrangements of filaments or chains inter-linked by reversible bonds, are omnipresent in both natural and synthetic materials. These materials range from thermally transient microemulsions[1] or molecular motor-driven microtubule networks,[2] to interlinked clusters of insects such as fire ants[3,4] or honeybees[5] at the macroscopic level. Reversible bonds in these networks tend to dissociate from stressed configurations and re-associate into relatively stress-free states, conferring dynamic networks with remarkable viscoelastic properties, including the ability to stress relax,[6] mitigate crack propagation,[7] and self-heal[8] at timescales governed by the underlying bond kinetics.[9] Relating the local chain properties and topologies of such networks to their global mechanical response is highly sought after by researchers aiming to elucidate the origins of biophysical phenomena,[10] as well as those interested in the predictive design of meta-materials with

suitably tough mechanical properties, the ability to self-repair,[11] or the ability to facilitate active transport.[12]

Towards this aim, many methods of modelling dynamic networks have been developed, including both microscale methods such as molecular dynamics (MD) or dissipative particle dynamics (DPD) simulations, and macroscale statistical mechanics approaches.[13] While the former methods simulate every elementary unit in a system (*e.g.*, atom, molecule or Kuhn segment) to predict the microstructural evolution with high precision,[14] they are computationally expensive. As such, modelling statistically representative volume elements (RVEs) – material unit cells that capture the full range of structural microphases – is often impractical when using these methods for amorphous materials. In contrast, continuum scale approaches such as the continuum model introduced by Hui *et al.* (2012)[15] or transient network theory (TNT)[9] manage to make a connection between bond kinetics and the emerging material response while requiring few computational resources. However, they usually rely on smoothing assumptions that restrict researchers from exploring the role of local heterogeneities or microstructural features. While statistical and computational approaches have been developed to relate damage to the macroscopic material response,[16,17] these models often remain bound to coarse-graining assumptions such as, isotropy, affine deformation and – commonly – idealized chains or bond dynamics. Isotropy is reasonably assumed for some, but not all,

Department of Mechanical Engineering, Program of Materials Science and
Engineering, University of Colorado, Boulder, USA.
E-mail: franck.vernerey@colorado.edu

dynamic networks,[7] whereas the affine assumption is typically violated at the network scale and slightly over-predicts stress.[18,19] Furthermore, assumptions of idealized chain force–extension models and constant bond dynamics are typically violated at intermediate to high chain stretches.[20–22]

To address these shortcomings, researchers have developed a number of multiscale models residing between the elemental length scale of MD simulations and material length scale of continuum approaches, which we will here refer to as the "mesoscale".‡ Rather than simulate the elemental units of a network, mesoscale models generally coarse-grain entire chains and prescribe their mechanical properties through statistical representations such as the ideal Gaussian model.[23] In doing so, these models avert high computational cost while still permitting investigation of the detailed microstructural changes that occur during network evolution.[13] Mesoscale models have been extensively used to study the effects of non-affine deformation in permanent networks,[24–26] revealing that the affine assumption limits continuum models' abilities to predict the mechanics of networks near the percolation threshold.[27] By extension, this also limits continuum models in cases where damage occurs during deformation.[7,17] In contrast, mesoscale models easily permit probabilistic rupture of bonds through models such as Eyring's[21] or Bell's[28] theory, while inherently tracking the topological evolution of the network. Such mesoscale methods may be applied directly to entire networks[29,30] or incorporated into "quasicontinuum" models[31–33] in which regions of high micro-structural interest (*e.g.*, those undergoing plastic deformation or damage) are examined mesoscopically, while elements of lower interest (*i.e.*, homogenous regions) are captured through statistical continuum models. Through both methods, researchers have employed mesoscale models in the examination of permanent damage, mechanical toughness, and loading rate-dependence, to determine how these features are affected by chain properties and concentrations.[30,32–34] A natural extension of such work is to then apply mesoscale modeling in the exploration of dynamic networks in which the dissociation of bonds is reversible. Indeed, researchers in the biophysics community have examined active dynamic systems such as actin–myosin or cytoskeletal networks using mesoscale modeling approaches.[10,22] However, inclusion of activity in these systems obfuscates the isolated effects of traits such as topology, chain properties, and bond kinetics, which researchers of thermally driven dynamic networks (*e.g.*, vitrimers[35,36]) are most immediately concerned with. In the study of inactive polymers with reversible bonds, other researchers have employed the more traditional methods of MD-Monte Carlo simulations to directly study[37] or develop specific statistical approaches in the study of features such as self-healing and adhesion of dynamic polymers.[38] However,

these methods are inhibited by the same computational costs and inaccessibility to larger time and length scales discussed earlier. Ergo, there remains much to be learned through the development and application of a general mesoscale framework for networks with reversible bonds.

Moving in this direction, we here introduce a discrete, mesoscopic, network model with dynamically cross-linking connections that may represent a broad scope of systems ranging from vitrimers[39] to gel networks.[40] Our main contribution is at two levels. First, we introduce the mesoscale model, which captures the time-dependent mechanical responses of networks with dynamic connections, and allows us to relate them directly to networks' topological evolution. This model incorporates not only probabilistic bond detachment, but also reattachment events, thus broadening the scope of networks that may be explored from permanent networks (with or without damage), to those that may flow and self-heal. In the first iteration of this model, we focus on networks of flexible chains permanently cross-linked to one another at one end in a star-like configuration and containing reversible binding sites at their free ends, which we will refer to as "stickers" (Fig. 1). As the first application of this model and second contribution of this work, we compare the predictions of this approach to those of the existing continuum TNT,[9] thereby allowing us to explore the limitations of the statistical approach directly as they relate to the underlying network properties and loading conditions. In the remainder of this manuscript, we briefly describe the TNT for dynamic networks of Gaussian chains, introduce the discrete model, and then explore the mechanical responses predicted by each of these methods.

2 Transient network theory for Gaussian networks

The TNT begins with the statistical treatment of networks comprised of randomly oriented flexible chains connected by reversible bonds with intrinsic association and dissociation rates, k_a and k_d, respectively. The elastic energy of these networks derives from the entropic elasticity of their connected
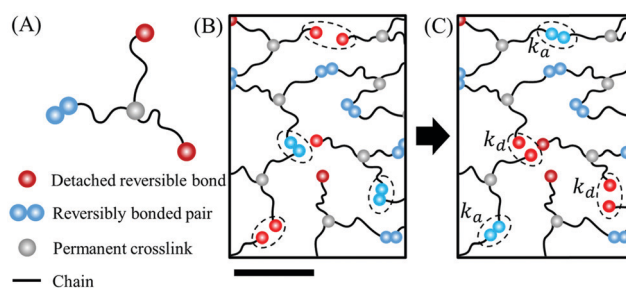

Fig. 1 (A) A single sample constituent with three possible attachments is shown. Per the legend, grey nodes represent permanent crosslinks, blue nodes represent reversibly bonded pairs, red nodes represent detached reversible bonds and black curves represent chains. (B and C) A sample network (B) before and (C) after a series of attachment and detachment events (denoted by k_a and k_d, respectively) is depicted. The scale bar represents approximately 1ζ where ζ is the characteristic spacing between permanent crosslinks in the network.

---

chains, which is expressed in terms of their end-to-end vectors $\boldsymbol{r}$. For a population of Gaussian chains, the most probable end-to-end distance or "reference state" is expressed by the product $\sqrt{N}b$, where N and b are the number and length of Kuhn segments in a chain, respectively.[20] For convenience, the physical state of a chain is taken as the stretch vector $\boldsymbol{\lambda} = \boldsymbol{r}/(\sqrt{N}b)$, such that $\boldsymbol{\lambda}$ is a unit vector when chains are in their reference state. To provide a statistical description of the network, one then introduces the distribution function $\phi(\boldsymbol{\lambda}, t)$ that characterizes the number density of chains found in configuration $\boldsymbol{\lambda}$. Since this distribution describes the physical state of the full population, it can be used to calculate important macroscopic quantities such as the elastic energy, stress, or viscous relaxation.[4,6,9]

Let us now consider a small network volume, subjected to an overall deformation history, characterized by the time-dependent deformation gradient tensor $\boldsymbol{F}(t)$. At a given time, this function can be used to evaluate the velocity gradient tensor through the relation $\boldsymbol{L} = \dot{\boldsymbol{F}}\boldsymbol{F}^{-1}$ where the superimposed dot represents the material time derivative. From this knowledge, it is possible to construct an evolution equation for the distribution function over time if a relationship is postulated between global deformation $\boldsymbol{L}$ and local chain deformation $\dot{\boldsymbol{\lambda}}$. The simplest and most common assumption is given by the instantaneously affine approximation[6] that reads $\dot{\boldsymbol{\lambda}} = \boldsymbol{L}\boldsymbol{\lambda}$. In this case, it can be shown that the material time derivative of the distribution takes the form of the Fokker–Planck equation:[9]

$$\dot{\phi} = -\boldsymbol{L} : \left(\frac{\partial \phi}{\partial \boldsymbol{\lambda}} \otimes \boldsymbol{\lambda}\right) - \phi \mathrm{Tr}(\boldsymbol{L}) + k_{\mathrm{a}} c_{\mathrm{d}} p_0 - k_{\mathrm{d}} \phi \qquad (1)$$

where c_{d} is the concentration of detached chains and $p_0(\boldsymbol{\lambda})$ describes the probability density function at which chains reattach to the network. The function $p_0(\boldsymbol{\lambda})$ is usually taken as an anisotropic, multivariate Gaussian with variance $\sqrt{N}b$ to express the fact that chains reconnect into a relaxed conformation. In this work, we concentrate on incompressible networks, characterized by $\det(\boldsymbol{F}) = 1$, or alternatively, $\mathrm{Tr}(\boldsymbol{L}) = 0$. This therefore implies that the second term on the right-hand side of eqn (1) vanishes in the remainder of this manuscript. Given the evolution of the chain distribution (ϕ) through eqn (1), and assuming the force–extension (f–λ) response of a single chain is known, the stress in the network can be directly evaluated through the virial formula as:[9]

$$\boldsymbol{\sigma} = \|\phi \boldsymbol{f} \otimes \boldsymbol{\lambda}\| + \pi \boldsymbol{I} \qquad (2)$$

where π is a hydrostatic pressure that enforces the network's incompressibility.

We here concentrate on a reduced form of the TNT,[41] where the chain distribution is described by its covariance matrix $\boldsymbol{\mu} = \frac{3}{c}\|\phi(\boldsymbol{\lambda})\boldsymbol{\lambda} \otimes \boldsymbol{\lambda}\|$, also known as the conformation tensor. Focusing on the case where the rates of chain dissociation k_{d} and association k_{a} are constants and independent of deformation, then the concentration of attached (and therefore detached) chains quickly reaches a steady state that is not affected by the loading history. This steady state concentration given by:

$$c = \frac{k_{\mathrm{a}}}{k_{\mathrm{a}} + k_{\mathrm{d}}} c_{\mathrm{t}} \qquad (3)$$

where c_{t} is the total chain density. Furthermore, the Fokker–Planck equation can be replaced by its reduced form, that describes the evolution of the conformation tensor as follows:[9]

$$\dot{\boldsymbol{\mu}} = \boldsymbol{L}\boldsymbol{\mu} + \boldsymbol{\mu}\boldsymbol{L}^{\mathrm{T}} - k_{\mathrm{d}}(\boldsymbol{\mu} - \boldsymbol{I}) \qquad (4)$$

If the network is initially stress-free, this equation is complemented by the initial condition $\boldsymbol{\mu} = \boldsymbol{I}$, where $\boldsymbol{I}$ is the identity tensor. It can be shown that a general solution of this equation is:[9]

$$\boldsymbol{\mu}(t) = \boldsymbol{F}\boldsymbol{F}^{\mathrm{T}}\mathrm{e}^{-k_{\mathrm{d}}t} + k_{\mathrm{d}}\boldsymbol{F}\left(\int_0^t \left(\boldsymbol{F}_\tau^{-1}\boldsymbol{F}_\tau^{-T}\right)\mathrm{e}^{-k_{\mathrm{d}}(t-\tau)}\mathrm{d}\tau\right)\boldsymbol{F}^{\mathrm{T}} \qquad (5)$$

where the deformation gradient $\boldsymbol{F}_\tau = \boldsymbol{F}(\tau)$. Although many flexible chains exhibit a severe, non-linear strain-stiffening response when deformed near their contour lengths, for simplicity, we here assume that the force–extension relation is that of a linear Gaussian chain taking the form $f = 3kT\lambda$ where kT is the thermal energy. In this case, the stress simplifies to:[9]

$$\boldsymbol{\sigma} = ckT\boldsymbol{\mu} + \pi \boldsymbol{I} \qquad (6)$$

Combining this equation with the general solution for the conformation tensor (eqn (5)) leads to the prediction of the stress tensor for an arbitrary deformation history $\boldsymbol{F}(t)$. The TNT has been amply used to understand the molecular origin of the viscoelastic response by transient networks.[4,6,9,42–45] It however hinges on a number of assumptions that could affect the validity and accuracy of its prediction in certain conditions. Among those assumptions are (a) the affinity of the chain deformation, (b) the assumption of constant association and dissociation kinetics, and (c) the linear force–extension response of the flexible chains. To explore these limitations, we here construct a discrete, transient network model that does not rely on these restrictions.

3 Discrete model of transient networks

The topology of transient networks can be very diverse. Without compromising generality, we here present a model that consist of a network of star-shaped units whose branches may reversibly bind with one another, in line with the depiction of Fig. 1. As a discrete model that represents the end-to-end vector of every chain, this framework inherently captures the non-affine response of the network as it undergoes conformational changes during deformation. Similarly, given bond dynamics, the framework also captures non-affine changes due to network reconfiguration. Furthermore, the bond dissociation rate of attached chains is prescribed a statistical dependence on force through Eyring's theory,[21] while the association rate of detached chains is governed by their proximity to neighboring open chains and their timescale of tethered Rouse diffusion,[38] thus rendering the

assumption of constant kinetic rates unnecessary. Finally, the chains are assigned a nonlinear force–extension relationship through the Padé approximation of Langevin chains,[46] capturing the enthalpic stiffening of chains from the stretching of intra-constituent bonds as they near full extension (as opposed to just entropic stiffness from unfolding).[47] In the remainder of this section, we detail the prescribed force–distance relationships (both the attraction of mutually bonded nodes due to chain forces and repulsion of neighboring nodes due to volume exclusion), bond kinetics (both detachment and attachment), and integration of single chains into a network.

3.1 Elastic and repulsive interactions in a transient network

Networks' constitutive properties are intrinsically tied to the constitutive properties of their elemental building blocks. Therefore, due consideration must be given to the assignment of a force–extension relationship, $f(\lambda)$, for jointly connected chains in the model. In many networks of flexible chains, a nonlinear stiffening occurs when members are stretched close to some finite contour length. To prescribe a finite contour length, we employ the Padé approximate for Langevin chains[46] for which the corresponding free energy is:

$$\mathscr{U}_{\mathrm{c}}(\lambda) = kT\left[\frac{\lambda^2}{2} - N\log(N - \lambda^2)\right]. \qquad (7)$$

Notably, the force in a Langevin chain diverges in the limit $\lambda \to \sqrt{N}$ (*i.e.*, $r \to L$), enforcing that $f \to \infty$ when the chains are stretched to their full contour length (Fig. 2A). This nonlinear divergence at high chain stretch is common to polymeric chains. In fully extended polymer chains, the conformational degrees of freedom are minimized and the stiffness of the chains is no longer entropically driven, rather it is governed by the much stiffer stretching of covalent bonds between monomers.[48]

This model relies on the freely-jointed assumption that there is no energetic penalty for changing the angle between adjacent chain segments (*i.e.*, bending). Employing freely-jointed chains simplifies our network model by eliminating moments on our permanent crosslinks, instead ensuring that the force from a chain always occurs pairwise and in-line with the centers of mass of the nodes to which it is connected. It also permits us to assume a circumferentially symmetrical radial distribution for unattached chains such that the stickers are equally likely to occupy any azimuth about their tethered node. However, with no energetic penalty for bending the chains have no finite rest length and are always in tension, which – in the absence of any repulsive potential – will cause traction-free networks to converge to a single point. To mitigate this non-physical effect, we introduce soft volume exclusion between permanent crosslinks through a generic inverse repulsion potential of the form:[49]

$$\mathscr{U}_{\mathrm{R}}(d) = \begin{cases} E\left[\gamma\left(\dfrac{d}{R}\right) + \left(\dfrac{R}{d}\right)^{\gamma}\right], & \text{if } d < R \\ 0, & \text{if } d \geq R \end{cases} \qquad (8)$$

where E is a characteristic energy scale, R is the effective particle radius, γ is a scaling parameter that defines how soft the particle is (where setting γ lower decreases the particle stiffness), and d is the pairwise separation distance between neighboring nodes' centers of mass. From eqn (8), we may derive the repulsive force according to $\partial\mathscr{U}_{\mathrm{R}}/\partial d$, which gives $f_{\mathrm{R}}(d) = \gamma E(1/R - R^{\gamma}/d^{(\gamma+1)})$ when $d < R$ while $f_{\mathrm{R}}(d) = 0$ otherwise. Thus, the total force acting between an adjacent set of bonded nodes becomes the sum of the tensile chain force and repulsive volume exclusion force. Ultimately, ε and R are set such that the net force between a bonded pair becomes zero at a distance of $R = 2l_{\mathrm{c}}$, which ensured that the networks always hosted some effective pressure from volume exclusion, and which led to negligible stress in equilibrated networks regardless of chain concentration (see Section 3.4). Additionally, γ is set to 2 in order to achieve a very soft pairwise repulsion. We set the contour length of an attached chain to $Nb = 3.5$ units of length, and assume monodispersity, which enforces that chains remain close to the linear regime of the tensile force when connected to nearest neighbors. Note that while the Langevin contribution to the pairwise force between nodes exists only if said nodes are mutually bonded, volume exclusion force is maintained between all nodes within the radial separation distance $d \leq R$, hence the distinction between center of mass separation distance "d" and chain end-to-end distance "r".

3.2 Force-dependent bond dissociation

At the constitutive level, the process of detachment is governed by the competition between the binding energy, ΔG, of reversible bonds and the force-dependent free energy, $\Psi(f)$, stored in the bonds' chains. If the free energy in the chain exceeds this binding energy ($\Psi(f) > \Delta G$), then the bond will detach while if the energy barrier is not eclipsed the bond will remain attached. As such, bond detachment is an inherently force-dependent phenomenon. In many of the systems modeled, such as polymeric networks, the force produced in a chain contains a random diffusion-governed, entropic contribution. Therefore,
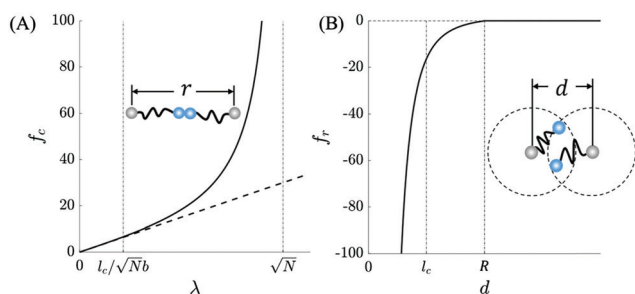

Fig. 2 (A) The entropic tensile force of an attached chain is plotted with respect to extension, $\lambda = r/\sqrt{N}b$. Both the Gaussian (dashed black line) and Langevin (solid black curve) chain models are displayed. The nominal spacing between nearest neighboring permanent crosslinks, l_{c}, and the chain contour length, $\lambda = \sqrt{N}$ are denoted for reference. (B) The repulsive force between neighboring units due to volume exclusion is plotted with respect to separation distance, d. Again, l_{c} is marked for reference. The length scale above which repulsion goes to zero, R, is also denoted.

the detachment process will appear probabilistic at the mesoscale and so we employ an average rate to describe random dissociation events.

One commonly employed statistical model for force-dependent detachment in both mesoscale[10] and continuum approaches[7] is Eyring's theory, which describes the average bond detachment rate k_d (or average inverse bond lifetime, $k_d = 1/\tau_b$) according to:

$$k_d = k_d^0 \exp\left(\frac{f x_d}{kT}\right), \tag{9}$$

where k_d^0 is the force-free detachment rate and x_d is the detachment activation length scale that characterizes the force-sensitivity through $f_0 = kT/x_d$.[21] The effects of force sensitivity are displayed in Fig. 3A. When f_0 is on the order of $20kT/b$, there is very little extension-dependence of k_d until $\lambda \to \sqrt{N}$. In contrast, when f_0 is on the order of $0.2kT/b$, k_d is more than tenfold greater than k_d^0 at the initial separation distance between nearest neighbors, l_c. As f_0 will greatly impact the connectivity and therefore stiffness of the networks in this model, further investigation into its effects may be considered in future work. However, here f_0 is held at $2kT/b$, which produces an intermediate force-dependent effect on k_d wherein f reaches f_0 at $r \approx 2.5l_c$. Regardless of f_0, under no applied load ($f = 0$), the stress-free rate of detachment due to random fluctuation is given by k_d^0. From eqn (9) we see that as force increases, the detachment rate increases exponentially. Referencing the force–extension relationship of attached chains (Fig. 2A) we see that the detachment rate diverges and the bond lifetime goes to zero in the extensile limit $r \to L$ (or $\lambda \to \sqrt{N}$). It should be noted that eqn (9) is also synonymous with the Bell model originally employed to predict slip bond detachment kinetics between cells,[28] thus generalizing its application beyond the systems Eyring originally studied.

To gauge the effects of this coarse-grained detachment algorithm on a single chain, we conduct a simple benchmark problem. Two chains whose reversible binding sites are initially attached, have their permanently cross-linked ends held apart

at some constant chain length, r. The nominal detachment rate, k_d, in this chain is then computed through eqn (9). From a numerical view point, the detachment kinetics of a detached chain can be seen as a stochastic process, where each event is considered independent. It can therefore be considered as a Poisson process with average rate k_d. The differential probability P_d for an attachment event to occur during a time interval t and $t + dt$ therefore follows the relation:

$$dP_d = k_d e^{-k_d t} dt. \tag{10}$$

Discretizing t by some small numerical timestep, Δt, and accounting for the memorylessness of the exponential function, we may rewrite this relationship such that the probability of detachment at any given timestep in the model is taken as:

$$P_d = 1 - e^{-k_d \Delta t}. \tag{11}$$

Time is stepped in increments of Δt, and a random number, a, in the range $a \in [0, 1]$ is checked against P_d. If, $a \leq P_d$, the bond is detached, the bond lifetime is recorded, and the simulation stops. This process is repeated for 20 000 observations over three separate values of r ($r = l_c$, $r = 2l_c$, and $r = 3l_c$). The resulting probability mass functions of bond lifetime are presented in Fig. 3B, which agree with the continuous distributions predicted by eqn (10). As r increases, the tail of the histogram shortens and the peak of the distribution increases indicating a shorter average bond lifetime for highly stretched chains, as expected from eqn (9). In contrast, decreasing r elongates the tail of the distribution and reduces the peak value, indicating that shorter chains have longer average bond lifetimes.

3.3 Kinetics of bond association

Let us now concentrate on estimating the lifetime of a dangling bond, that is attached to a fixed node as shown in Fig. 4A. While other researchers have successfully employed Bell's theorem for the reattachment of bonds that fasten together "hidden lengths" or phantom loops,[50] this approach requires that the reversible bonds reside along the lengths of the polymers and that the chains remain intact, albeit elongated, after bond rupture. However, bond breakage in the networks examined here results in complete chain scission and the formation of two dangling chains, which are tethered only at one end to their permanent cross-links. Under such conditions, assuming negligible long-range potential between the free stickers and that the bond transition length scale is very small (such that bonds reform when two free stickers effectively come into contact), then bond association kinetics depend primarily on the diffusion of detached stickers. When detached, a dangling flexible chain explores the space surrounding the central node through a sub-diffusive Rouse process. Following Stukalin *et al.* (2013),[38] and assuming sufficiently flexible, ergodic chains, we designate τ_0 as the time it takes for this bond to move through the molecular distance b. This time depends on both temperature and the friction coefficient between the dangling chain and its surrounding medium. Following the Rouse diffusion model, the mean square
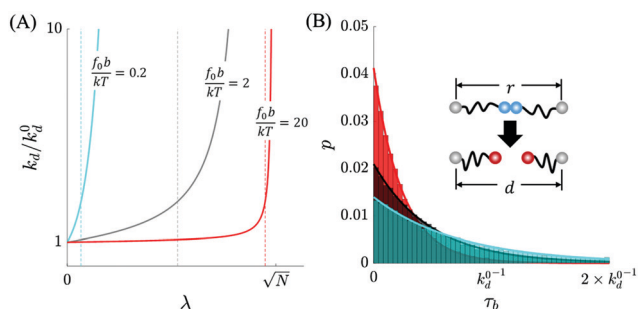

Fig. 3 (A) Rate of unbinding as a function of chain stretch is plotted for three different values of bond force sensitivity, f_0. The vertical dashed lines represent the stretches at which $f = f_0$ (or $k_d = e$) for each value of f_0. (B) Statistics of the bond lifetime of an attached chain when $f_0 = 2kT/b$, are plotted for three different values end-to-end distance, r: $r = l_c$ (cyan), $r = 2l_c$ (black), and $r = 3l_c$ (red), where l_c is nominal spacing between nearest neighboring permanent cross links.
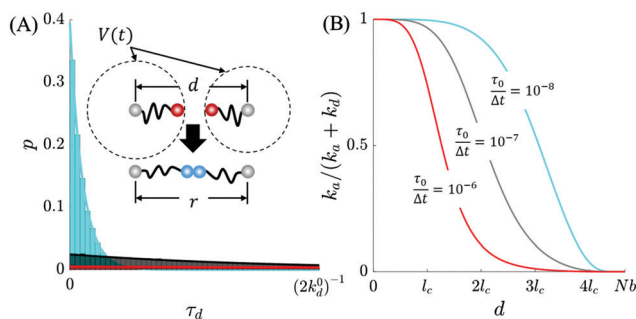
Fig. 4 (A) Statistics of the free sticker lifetime are plotted for three different values separation distance, d: $d = l_c$ (cyan), $d = 2l_c$ (black), and $d = 3l_c$ (red), where l_c is nominal spacing between nearest neighboring permanent cross links. (B) $k_a/(k_a + k_d)$ is plotted with respect to separation distance, d, for three different values of the diffusion sticker timescale, τ_0, which predicts the fraction of chains that will be attached at a given value of d (f_0 is held at $2kT/b$).

displacement $\langle \Delta r^2(t) \rangle$ of the dangling bond around its anchoring node increases as a square-root of time following:

$$\langle \Delta r^2(t) \rangle = b^2 \sqrt{t/\tau_0}, \qquad (12)$$

for $\tau_0 < t < \tau_R$, where τ_R is the Rouse time of the dangling chain given by $\tau_R = \tau_0 N^2$. Let us now estimate the three-dimensional volume V explored by the bond over time (Fig. 4A). This volume may be estimated by the mean square displacement as $V(t) = \langle \Delta r^2(t) \rangle^{3/2}$, which, combined with eqn (12) yields the relation:

$$V(t) = b^3 (t/\tau_0)^{3/4}. \qquad (13)$$

To obtain a scaling law for the average lifetime of a free dangling chain, we postulate that a binding event occurs when the exploration volume $V(t)$ is equal to the volumes at which two dangling chains, attached to nodes separated by a distance d, intersect (i.e., $V \approx d^3$). Applying this to eqn (13) gives the average life time of a free dangling chain as $\tau \approx \tau_0(d/b)^4$. In other words, the average rate of association $k_a = 1/\tau$ scales nonlinearly with the distance between two nodes according to the power law:

$$k_a \approx \frac{1}{\tau_0} \left(\frac{b}{d} \right)^4, \qquad (14)$$

where $k_a = 0$ if $d > Nb$. Note that this scaling law based on the work of Stukalin *et al.* (2013),[38] yields a rough estimation of the lifetime of a dangling chain and may be improved in a number of ways. For instance, the recombination of two dangling chains that belong to the same node is not considered here, but is expected to decrease the lifetime of these free chains. While this work ignores such effects for clarity, they may be included in ulterior versions of the model.

As with the detachment kinetics, the recombination kinetics of two dangling chains may be viewed as a stochastic process, where each event is independent, thereby being treated as a Poisson process with average rate k_a. Thus, the differential probability P_a of an attachment event occurring during the time interval t and $t + dt$ follows the relation:

$$dP_a = k_a e^{-k_a t} dt, \qquad (15)$$

where k_a is a function of both time and chain separation through eqn (14). Therefore, to gauge the effects of this coarse-grained attachment process on a single chain, we conduct another simple benchmark problem. As with the detachment process, we discretize t, giving the attachment probability within a discrete timestep as $P_a = 1 - e^{-k_a \Delta t}$. Two detached tethers separated by a fixed distances of $d = l_c$, $d = 2l_c$, and $d = 3l_c$ are allowed to bond and their unbound lifetime is recorded. The resulting probability mass functions from 20 000 detached lifetime observations each, are presented in Fig. 4A, which agree with the continuous distributions predicted by eqn (10). As d decreases, the tail of the histogram shortens significantly and the peak of the distribution increases indicating a shorter average unbound lifetime between nodes in close proximity, as expected from eqn (14). In contrast, increasing d lengthens the tail of the distribution and decreases the peak value, indicating an increased average unbound lifetime, with very few attachment events occurring at any given lifetime when $d = 3l_c$ in the observed time interval.

The combined effects of $k_a(d,t)$ and $k_d(r)$ are illustrated in Fig. 4B by plotting the ratio $k_a/(k_a + k_d)$ with respect to node separation distance d (which is synonymous with r for bonded nodes). This ratio predicts the steady state fraction of chains that will be attached at a given end-to-end distance. It remains close to one for small separations at which k_d will diminish (Fig. 3B) and k_a will increase (Fig. 4A). Similarly, it approaches zero in the limit $r \to Nb$. To also highlight the effect of the sticker diffusion timescale, Fig. 4B displays $k_a/(k_a + k_d)$ for three values of τ_0: $\tau_0 = 10^{-6}\Delta t$, $\tau_0 = 10^{-7}\Delta t$, and $\tau_0 = 10^{-8}\Delta t$. When τ_0 is increased (i.e., when it takes longer for the sticker to travel a distance b), the fraction of attached chains at a given distance generally decreases, as expected given the corresponding reduction in k_a through eqn (14). Specifically, when $\tau_0 = 10^{-8}\Delta t$, the fraction of attached chains remains close to one until $d > 2l_c$, while when $\tau_0 = 10^{-6}\Delta t$, the fraction of attached chains only remains close to one when $d < l_c$. As with f_0, τ_0 greatly impacts the connectivity and therefore mechanical properties of the networks. In the scope of this work, τ_0 is set to $10^{-7}\Delta t$, such that the predicted fraction of attached chains transitions from one to zero within the approximate node separation range of this model ($l_c < d < 4l_c$) (see Fig. 4B).

3.4 Network model and algorithm

To explore the mechanical response of transient networks, we here concentrate on two-dimensional, plane stress RVEs with periodic boundary conditions (Fig. 5). The details of applied periodic boundary conditions are provided in the ESI.† For simplicity, these RVEs are initially square domains Ω_0 that contain star-shaped units (with n dangling chains) whose centers (nodes) act as permanent cross-link sites (Fig. 1). The free ends of the dangling chains each possess a sticker that can reversibly connect to the dangling chains of neighboring units as discussed above. While many branched dynamic networks include reversible binding sites along the intermediate length
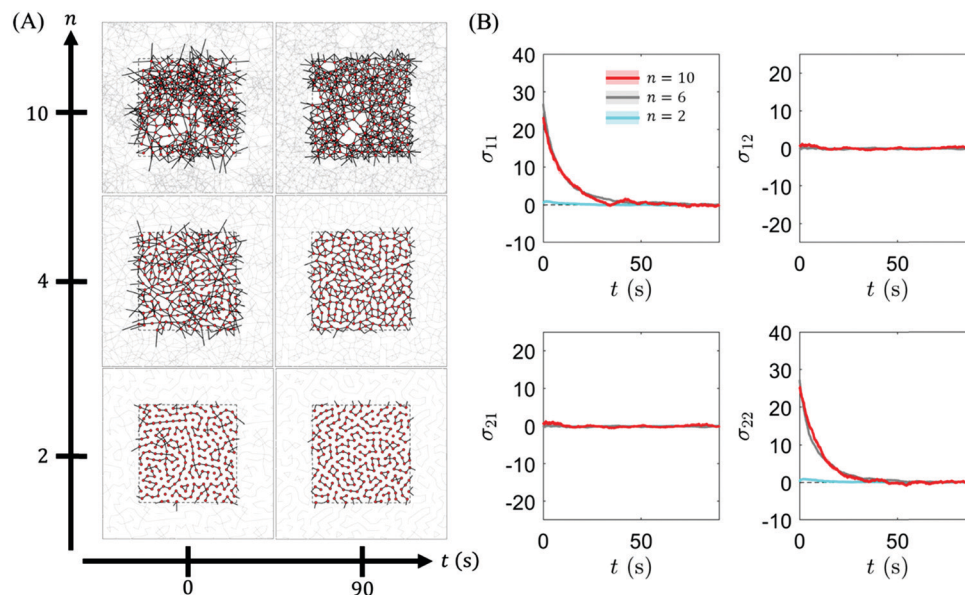
Fig. 5 (A) Snapshots of networks with $n = 10$ (top row), $n = 4$ (middle row) and $n = 2$ (bottom row) are shown at initiation (left column) and at the end of a 90 second dynamic equilibration process (right column). Red dots represent permanent crosslink sites and black lines represent connected chains. Grey lines represent the periodically replicated chains. Note that permanent crosslinks are reduced in size for visual clarity when plotted. (B) The four components of in-plane virial stress are plotted with respect to time.

of their structural chains,[30,51,52] we here focus on star-shaped units because it allows us to begin by comparing TNT to the relatively simple case of a monodisperse network with a comparatively homogeneous cross-link distribution. We next describe the numerical approach used to explore the mechanical behavior of these transient networks.

3.4.1 Network generation. To generate the networks, $\mathcal{N}$ nodes are initially positioned within the domain Ω_0 at Cartesian coordinates $\boldsymbol{X}^\alpha$ ($\alpha \in [1, \mathcal{N}]$). For computational efficiency, the number of nodes included in the RVEs is set to $\mathcal{N} = 225$, such that minimum domain width at full deformation remains larger than the contour length of a single chain, thus ensuring that a chain cannot simultaneously span opposite boundaries of the RVE. Increasing the domain size further induces no change in global network stress (see ESI† for details). To ensure a uniform node distribution, node placement follows a 2D Poisson's point process originating at the domain's center ([0, 0]). The initial network configuration is then achieved by randomly linking chains according to the kinetics of bond association and dissociation described in the previous sections. The chain concentration c_t is tuned in this process through the number n of dangling chains assigned to each node. For simplicity, we posit here that two chains branching from the same node cannot form a connection. To enforce periodicity of the network, nodes across opposite domain boundaries are also allowed to connect and disconnect, as if neighboring one another. Note that in this coarse-grained approach, the dangling chains and stickers themselves are not explicitly modeled when detached. Rather, when a connection forms between cross-link α and its neighbor β, a chain of length Nb and end-to-end vector $\boldsymbol{r}^{\alpha\beta} = \boldsymbol{x}^\beta - \boldsymbol{x}^\alpha$ is regarded with some resultant pairwise force, $\boldsymbol{f}^{\alpha\beta}$, acting on cross-link α due to β. In the simulations, we therefore only

visually represent the chains when they form connections between nodes.

Prior to applying any deformation, the initiated networks are dynamically equilibrated until they reach steady state. Here steady state is defined by equilibration of the network stress (Fig. 5), defined in Section 3.4.3. It should be noted that other benchmarks for steady state, such as the average number of connections Z per node or mean orientation of the chain end-to-end distribution, consistently stabilized before network stress.

3.4.2 Applying deformation. In this work, a global, but periodic network deformation is applied over time by imposing a macroscopic deformation gradient $\boldsymbol{F}(t)$. For this, the initially square window is deformed by updating the coordinates of its corners *via* the mapping

$$x_j(t) = F_{ij}(t)X_i \tag{16}$$

where x_j and X_i are the component of the corner points of the domain in their current and initial configuration, while F_{ij} are the components of the applied deformation gradient. For the purposes of this work, no shear components of $\boldsymbol{F}$ are applied, such that the window always remain orthogonal. The distortion of the window affects the distance between periodic pairs of nodes on opposite boundaries, thus triggering traction forces at the domain bounds. The deformation gradient $\boldsymbol{F}(t)$ is stepped in time increments of Δt, which is set such that k_d^{-1}, k_a^{-1}, and the inverse of the applied strain rate $\dot{\varepsilon}^{-1}$ are all at least two orders of magnitude higher than Δt and a maximum average of one stress free detachment event would occur for every one hundred tethers within a discrete time step (see ESI† for details). This ensures that the network configuration due to bond dynamics and conformation due to non-affine

deformation modes are updated with ample frequency as deformation is applied.

3.4.3 Network deformation and stress calculation. After the deformation is stepped, the unbalanced traction forces at the boundaries trigger the motion of nodes in the network until they reach their next equilibrium state. Force equilibration is achieved using a forward Euler, steepest descent algorithm.[53] Thus, the position of node α at iteration k, $\boldsymbol{x}_k^\alpha$, is updated according to:

$$\boldsymbol{x}_{k+1}^\alpha = \boldsymbol{x}_k^\alpha + \eta^{-1}\boldsymbol{f}_k^\alpha, \qquad (17)$$

where $\boldsymbol{f}^\alpha = \sum_\beta \boldsymbol{f}^{\alpha\beta}$ is the unbalanced force acting on node α, and η is simply a numerical overdamping coefficient set such that the residual force converges towards zero. Note that $\boldsymbol{f}^\alpha$ is inclusive of the tensile chain forces, as well as the repulsive volume exclusion forces. No random force due to Brownian noise is included in the scope of this work as the size of the units considered are such that isotropic noise will have a negligible net effect on diffusion. In contrast, the size of the tethered stickers is not large enough to mitigate Brownian noise, and therefore thermal noise is lumped into the kinetic rates of bond dynamics.

Iteration of eqn (17) proceeds until the unbalanced forces nearly vanish for all nodes. To reduce the computational cost without a significant reduction in accuracy, the threshold for the maximum and mean residual unbalanced forces are set to less than 5% and 2.5% of kT/x_d, respectively. We note here that force equilibration is assumed to occur significantly faster than the timescale of bond kinetics or applied deformation, such that neither bond dynamics nor applied deformation are updated during this procedure. At the end of each equilibration step, the stretched state of chains along with pairwise volume exclusion interactions culminate in some average true stress, $\boldsymbol{\sigma}$, which is computed using the virial formulation given by:

$$\sigma_{ij} = \frac{1}{2V} \sum_\alpha^{\mathcal{N}} \sum_\beta r_i^{\alpha\beta} \otimes f_j^{\alpha\beta}, \qquad (18)$$

where V is the domain volume.[54] We here exclude the inertial term of the virial stress commonly seen in atomistic or molecular scale discrete models, (due to the overdamped assumption which invokes that the nodes' inertia are negligible) and instead use the virial formulation inherent to the continuum model (eqn (2)).

3.4.4 Bond dynamics. After force equilibration, bond dynamics are enabled following the algorithms for attachment and detachment described earlier. Note that the networks examined are non-associative, in that the number of attached chains need not be conserved (i.e., bond exchange reactions are not prerequisite for dynamics to occur). The algorithm repeats the three steps described above (applying deformation, equilibrating network force, and updating network configuration due to bond dynamics) until the network has undergone the full prescribed deformation history.

4 Results

Here we report the predicted statistical and mechanical responses of discretely modeled transient networks, and compare them to those predicted by the TNT. Two main mechanical signatures are explored: (a) the rate-dependence of the network response and (b) the dynamics of its stress–relaxation. To achieve this, RVEs containing $\mathcal{N} = 225$ permanent cross-links are deformed per the load history described as follows and plotted in Fig. 6A:

• In the first stage, a uniaxial stretch is applied at constant true strain rate $\dot{\varepsilon}$ up to a stretch of 100% (Fig. 6A–D-0–2). Deformation is applied in the Cartesian basis $\{\boldsymbol{e}_1,\ \boldsymbol{e}_2\}$ (Fig. 6D) through the deformation gradient $\boldsymbol{F} = \mathrm{diag}(F_{11}, F_{22})$. The constant strain rate is achieved through the relation $F_{22}(t) = \exp(\dot{\varepsilon}t)$ and incompressible deformation is enforced through the condition $F_{11} = 1/F_{22}$ (i.e., $\det \boldsymbol{F} = 1$).

• In the second stage, a relaxation regime ensues in which the stretch is held constant until equilibrium is achieved (Fig. 6A–D-2–4).

In the loading regime, the solution of the TNT given by eqn (5) can be estimated numerically over time. In the relaxation regime, the deformation gradient remains constant and the solution eqn (5) takes the simple form:

$$\boldsymbol{\mu}(t - t_0) = \boldsymbol{\mu}_0 e^{-k_d(t-t_0)} \quad t \geq t_0 \qquad (19)$$

where t_0 is the final loading time (i.e., when relaxation begins) and $\boldsymbol{\mu}_0 = \boldsymbol{\mu}(t_0)$ is the conformation tensor at t_0. Eqn (19) predicts that the stress decays exponentially to zero with a decay rate of k_d (Fig. 6B-2–4). The TNT also provides a general representation of the chain statistics during network deformation. Since only axial stretches are applied here, the conformation tensor remains diagonal with components $\boldsymbol{\mu} = \mathrm{diag}(\mu_1, \mu_2)$. As discussed in Vernerey et al. (2017),[9] this tensor can be represented by an ellipse with semi-axes μ_1 and μ_2 in the directions $\boldsymbol{e}_1$ and $\boldsymbol{e}_2$, respectively. This ellipse represents the normalized mean-square stretch of the chains in different orientations (Fig. 6C). To produce statistically representative results from the discrete model, each of these conditions is imposed onto an ensemble of fifty different networks from which the average stress responses and chain distributions are measured. These results are illustrated in Fig. 6 for a reference network, with a chain concentration of $c \approx 15\zeta^{-2}$ (or average connectivity $Z \approx 8.4$), deforming at a strain rate $\dot{\varepsilon} = k_d^0$. Good agreement with the continuum prediction is obtained when the dissociation rate used in the TNT matches the average bond dissociation rate, $\bar{k}_d$, measured from numerical results ($\bar{k}_d \approx 6.5k_d^0$). Here, $\bar{k}_d$ is taken as the total number of detachment events in the network per time step, normalized by the total number of attached chains at the beginning of said time step. Significantly, the observation that $\bar{k}_d \neq k_d^0$ is a consequence of force-dependent detachment through eqn (9). In the remainder of this work, the applied strain rate is normalized by the rate $\bar{k}_d$, thus introducing the non-dimensional Weissenberg number $W = \dot{\varepsilon}/\bar{k}_d$.

Both the stress response in time, $\boldsymbol{\sigma}(t)$ (Fig. 6B) and the distribution functions of connected chains' end-to-end vectors,
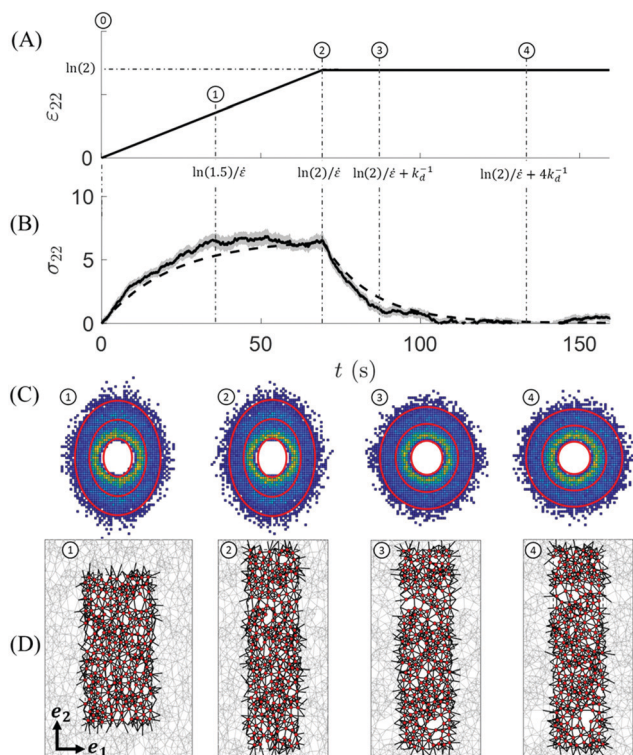
Fig. 6 (A) True strain in the direction of extension, $\varepsilon_{22} = \ln F_{22}$, is plotted with respect to simulation time. Loading is applied at a constant true strain rate until the network is stretched by 100% (*i.e.*, until time $t = \ln(2)/\dot\varepsilon$), after which the network is held in its deformed state until the stress fully relaxed. (B) The normal component of virial stress in the vertical direction is plotted with respect to time when $W \approx 1/6$ and $c \approx 15\zeta^{-2}$. The stress response shown is the ensemble average of 50 numerical experiments. Standard error, plotted as a shaded area around the curve, constitutes less than 5% of the mean. The stress response computed from (5) is plotted as a dotted curve. (C) The ensemble joint distributions of $r^{\alpha\beta}$ from ten numerical experiments are displayed as 2D histograms. r, as predicted by $r = \mu r_0$, is plotted as red ellipses for initial end-to-end lengths of $|r_0| = [0.5, 1, 1.5]$. (D) Snapshots of one numerical network during deformation are displayed for reference. (C and D) The designations 1–4 represent the network (1) at a stretch of 1.5, (2) at a stretch of 2 when loading is initially halted, (3) at time $t = k_d^{-1}$ into stress relaxation, and (4) time $t = 4k_d^{-1}$ into stress relaxation.

(Fig. 6C) are reasonably well-predicted by eqn (6) for the conditions given ($W \approx 1/6$ and $Z \approx 8.4$). Generally, during loading, chains are stretched in the direction of applied tension as indicated by the elongation of the joint distribution functions in Fig. 6C-1–2, resulting in the generation of tensile stress in the loading direction (Fig. 6B-1–2). Once loading is ceased (Fig. 6A–D-2–4), the joint distribution begins to revert to an isotropic state (Fig. 6C-3) and the stress relaxes (Fig. 6B-3). Eventually, the network reverts fully to the stress-free, isotropic state associated with $\mu_0 = I$.

It is however worthwhile to note that some deviation occurs during both the loading and stress relaxation phases. In the stress predicted by the discrete model is initially slightly greater than that predicted by eqn (6), likely due to the divergence of force associated with Langevin chains, which is not captured by the idealized continuum model. Yet, despite this initially higher stiffness, we see that the peak stresses at the time when

loading is ceased (Fig. 6B-2) roughly coincide between the discrete and continuum models. This is because a region of roughly steady state stress (*i.e.*, creep) is predicted by the discrete model in later loading stages. This stress plateau is not observed in the continuum model whose modulus always remains finite in the deformation range depicted. Notable discrepancies also exist during the stress relaxation regime, where the initial reduction in stress occurs faster for the discrete model than it does for the continuum model, indicating that the stress of the former does not decay exponentially. Both the creep response and non-exponential stress–relaxation of the discrete model may be attributed to three main mechanisms not captured by the continuum model: (a) non-affine micro-structural deformation, (b) nonlinear chain response, and (c) force-dependence of the bond dissociation rate k_d. While the observed differences are mild given the low loading rate ($W <$ 0.5) and high connectivity ($Z \gg 2$) presented in Fig. 6, we now explore the conditions under which the continuum model fails to capture the network mechanics predicted by the discrete model.

4.1 Effects of strain rate

To better understand the limitations of the TNT with regards to strain rate, we first sweep $W \in [1/8, 1/4, 1/2, 1, 2]$, while holding the total chain concentration c_t constant (therefore holding a fixed connectivity $Z \approx 8.4$). The global mechanical stress responses of networks loaded at various strain rates are displayed during deformation and relaxation in Fig. 7A and B, respectively. To elucidate the underlying micro-mechanical phenomenon that drives deviation in global stress between the continuum and discrete model predictions, the constant and stretch-dependent detachment rates (k_d), of a single chain in the continuum and discrete models, respectively, are plotted with respect to r in Fig. 7E. The percent deviation between the values of k_d from each model are also plotted with respect to r in Fig. 7E, to show that k_d of highly stretched chains deviates significantly between the models. The maximum values of k_d at four different times corresponding to (1) partway through loading, (2) at peak loading, (3) partway through stress relaxation, and (4) near complete stress relaxation are denoted for the lowest (blue) and highest (red) strain rates, respectively.

4.1.1 Nonlinear Langevin chains stiffen the network response during initial loading. It is well-known that the affine assumption leads to over-prediction of true stress; however the results depicted in Fig. 7A show that during the initial loading, the stress predicted by the TNT is consistently underestimated across all strain rates. This is not observed for discrete networks of Gaussian springs (see Fig. S1, ESI†). It is therefore attributed to the use of Langevin chains in the discrete model, whose force, as modeled through the Padé approximation,[46] not only exceeds that of ideal chains at any stretch (albeit, minutely below $\lambda = l_c/\sqrt{N}b$), but also undergoes divergence as chains are stretched to their contour lengths (Fig. 2A). As such for fixed values of N, b and c_t, the Langevin chain model always produces networks with higher predicted stiffness than those comprised of linear chains and the effect is exacerbated at high
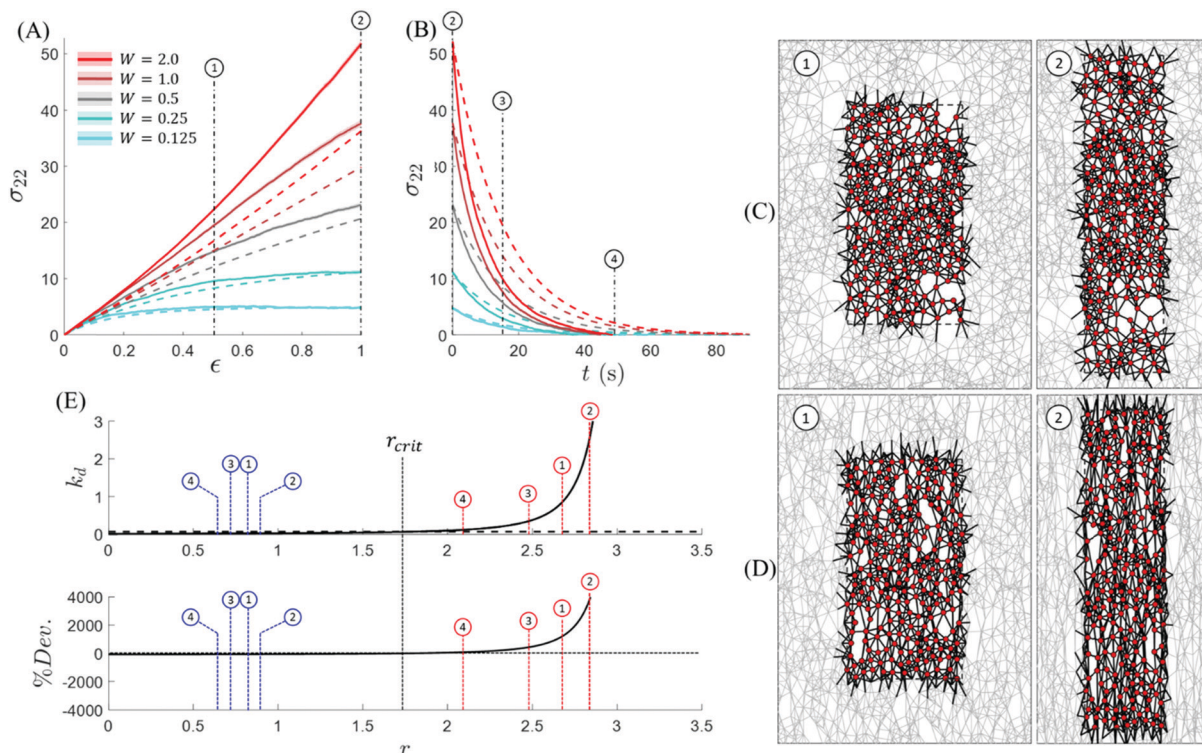
Fig. 7 (A) Normal stresses from creep experiments are plotted with respect to engineering strain, $\varepsilon = F_{22} - 1$, for $W \approx 1/8$ (cyan), $W \approx 1/4$ (teal), $W \approx 1/2$ (grey), $W \approx 1$ (maroon), and $W \approx 2$ (red). (B) Normal stresses from relaxation experiments are plotted with respect to time for three different initial values of stress. All results from the discrete model are plotted as continuous curves with standard error represented by the shaded region, and results from TNT are plotted as dotted curves. (C and D) The corresponding networks at times 1 (left) and 2 (right) are depicted when (C) $W \approx 1/8$ and (D) $W \approx 2$ to highlight the effect of strain rate on chains' stretches and orientations. (E) Top: Bond dissociation rate, k_d is plotted with respect to r for Erying's theory employed in the discrete model (continuous black curve) and the constant k_d assumption used in the continuum model (dotted black line). Bottom: the percent deviation between the continuum and discrete model dissociation rates is plotted with respect to r. Where the percent deviation transitions from negative to positive is labeled r_{crit}, as chains with $r > r_{crit}$ will undergo faster dissociation than predicted by the continuum model. The four values denoted in blue represent the average values of r for times (1–4) when $W \approx 1/8$. Similarly, the four values denoted in red represent the maximum values of r for times (1–4) when $W \approx 2$.

stretches. Therefore, the continuum model should always under-predict the network stress, regardless of the loading history. Yet, the stress responses during the relaxation regime in Fig. 7B indicate that this is not the case.

4.1.2 Network connectivity is conserved despite force and separation-dependent bond dynamics. Given force-dependent detachment through eqn (9), we find that there exists an increase in the mean detachment rate, $\bar{k}_d$, during deformation. This is exemplified in Fig. 7E (for the case of $W \approx 1/2$) by the slight increase of the mean during times of loading (designated by the blue tags labeled "1" and "2"), *versus* times of relaxation (denoted by the blue tags labeled "3" and "4"). The increase in mean detachment rate during deformation is negligible for low strain rates (*e.g.*, $W \approx 1/8$), but as high as 15% for high strain rates (*i.e.*, $W \approx 2$) immediately highlighting a limit of the constant k_d assumption when applied to networks undergoing fast loading. Even more pronounced is the impact of high loading rate on the maximum value of k_d for a single bond. In the case of $W \approx 1/2$, some bonds became stretched enough to undergo a forty-fold increase in k_d over the mean effective value used to fit the continuum model, which occurred during peak loading (designated by the red tag labeled "2"). Later we

examine how local increase in k_d impacts the networks' stress response during loading and relaxation; but first we note that escalation of k_d drives a corresponding increase in the mean attachment rate, $\bar{k}_a$, which is taken as the total number of attachment events in the network per time step, normalized by the total number of detached chains at the beginning of said time step. The increase in $\bar{k}_a$ is attributed to an increase in the number of attachment opportunities that occur at high strain rates due to both the higher detachment rate of chains and the mutual introduction of yet unattached tethers into each other's fields of reach. Despite this rise in bond reaction rates, the average connectivity $\bar{Z}$ of the network remains constant. This suggests that $\bar{k}_d$ and $\bar{k}_a$ increase proportionally such that the steady state concentration predicted by eqn (3) remains valid for all deformation rates observed. Nevertheless, the increased bond kinetics act as a softening mechanism whose effects, as discussed below, are most pronounced at higher strain rates.

4.1.3 Force-dependent bond detachment entails non-exponential stress relaxation. The most obvious effect of force-dependent detachment is the non-exponential decay of stress which occurs during relaxation as observed in Fig. 7B. More specifically, once loading is ceased, the discrete network

stress initially decays faster than the continuum model predicts and the degree of disagreement is greater for larger stresses (as in the case of higher loading rates). To understand this response, we examined the percentage of chains whose end-to-end distances r, exceeds the value at which the local detachment rate equals that of the value fitted to the TNT, r_{crit} (Fig. 7E). As expected, Fig. 8A and B demonstrates that this percentage is generally higher during loading (at times "1" and "2") than during relaxation (at times "3" and "4"), and this effect is more pronounced for higher strain rates. This increased percentage of highly stretched chains explains the non-exponential decay of stress in the direction of applied loading for a few reasons. Firstly, the non-linearity of eqn (9) ensures that the bond dissociation rates of chains stretched beyond r_{crit} are orders of magnitude higher than those of bonds in the regime $r < r_{crit}$. Thus, the bonds detaching more frequently are those which are highly stretched, which – given any monotonically increasing force–extension relationship – are also those carrying the most tensile load and thus disproportionately contributing to the global stress response.

Secondly, this effect is exacerbated by the use Langevin chains, which ensures that not only are the highly stretch chains contributing disproportionately to the stress, but they do so non-linearly due to the divergent chain force in the limit $\lambda \rightarrow \sqrt{N}$. Finally, as illustrated through the joint distribution functions of r (Fig. 8C), the majority of chains stretched past a distance of r_{crit} are oriented with their larger component in the direction of global stretch (e_2); therefore, as these chains detach, they will principally reduce the reported stress component σ_{22}. While these effects are most noticeable during stress–relaxation, closer examination also reveals that they impact the stress response observed during loading as well.

4.1.4 Force-dependent bond dynamics begets steady-state creep regardless of strain rate. Under the assumption of a constant dissociation rate k_d, the TNT predicts that a network subjected to a constant true strain rate (characterized by W) will experience a steady-state true tensile stress of the form:

$$\sigma = ckT\frac{W}{(1+W)(1-2W)}, \qquad (20)$$

which notably diverges when $W \geq 0.5$. This result can readily be obtained by setting the term on the left-hand side of eqn (4) to zero. In other words, when $W \geq 0.5$, the rate of energy dissipation due to chain detachment is overtaken by the rate of elastic storage due to deformation, such that the elastic energy increases infinitely with time. However, as displayed by Fig. 8D, discrete networks isochorically stretched to 250% of their original length do not exhibit such a singularity. Instead, the discrete model predicts that steady state creep is reached for strain rates up to $W = 1$. This observation is attributed to the stretch-dependency of k_d. Indeed for networks that are stretched slowly ($W \approx 0.1$) the percentage of chains exceeding r_{crit} remains close to 1% (Fig. 8A and B, cyan curve) throughout deformation while for networks that are stretched quickly ($W \approx 1$), the percentage of chains exceeding r_{crit} can reach close to 15% (Fig. 8A and B, maroon curve). The faster dissociation rate of these highly stretched chains mitigates storage of elastic energy such that a finite steady state stress is always observed. We note that steady state could not be reached for networks stretched at high rates without introducing exceedingly large Lagrangian deformation of the unit cell and so W is limited to the regime $W \leq 1$ with the given deformation approach. It is however expected that a steady creep will be obtained for any value of W based on the above analysis. Worth noting, is that at times the networks are observed to undergo a drop in stress rather than achieving steady state. Such cases occur when voids nucleate in regions of initially lower chain concentration, as exemplified by Fig. 8E.

Here, we define a void as a gap in the network's cross-link distribution whose characteristic height and width are both too large to permit locally sustained percolation. This occurs when the rate of attachment across said gap is an order of magnitude less than the corresponding rate of detachment (i.e., $k_a/(k_a + k_d) \lesssim 10\%$), which – referencing Fig. 4B – corresponds to a node separation of roughly $3l_c$. Therefore, although voids will not assume perfectly circular geometries, we loosely classify voids as vacant regions whose areas, A_v, satisfy the normalized
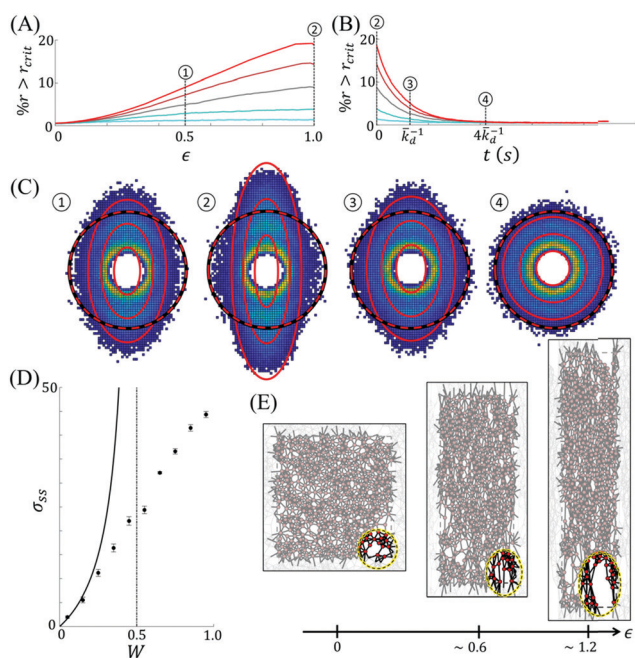

Fig. 8 (A and B) The percentage of chains stretched above r_{crit} during (A) creep and (B) stress relaxation is plotted with respect to engineering strain and time, respectively. Results from three values of true W: $W = 1/8$ (cyan), $W = 1/4$ (teal), $W = 1/2$ (grey), $W = 1$ (maroon), and $W = 2$ (red) – are shown. (C) The ensemble joint distributions of r from ten numerical experiments are displayed as 2D histograms for $W = 2$. r, as predicted by $r = mr_0$, is plotted as red ellipses for initial end-to-end lengths of $|r_0| = [0.5, 1, 1.5]$. r_{crit} is plotted as a red dashed circle to visually illustrate the fraction of chains that are above or below the threshold, as well as their orientation. (D) Steady state stress is plotted with respect to W for the numerical model as discrete data, and the continuum theory as a continuous black curve. The vertical dotted line at $W = 0.5$ denotes where the steady state stress predicted by the continuum model diverges. (E) A network deforming at a rate of $W = 0.85$ is depicted at three different strains and highlights a region where the local void nucleation occurs.

condition $A_v^* = A_v \Big/ \left[\pi\left(\frac{3}{2}l_c\right)^2\right] \geq 1$. Given this definition, transient voids appear to occur at every strain rate despite incompressible loading conditions. However, preliminary results suggests that voids constitute a greater average areal fraction, $\bar{\varphi}$, of the networks when high strain rates are applied (e.g., $\bar{\varphi} \approx 1.3 \pm 0.5\%$ when $W \approx 0.125$, whereas $\bar{\varphi} \approx 2.5 \pm 0.5\%$ when $W \approx 1$). This increase in $\bar{\varphi}$ emerges from a concurrent increase in the maximum number of voids observed existing simultaneously (n_v), average void area ($\bar{A}_v^*$) and average void lifetime ($\bar{T}_v$). Specifically, $n_v = 3$ *versus* 1, $\bar{A}_v^* = 1.67 \pm 0.20$ *versus* 1.36 ± 0.1, and $\bar{T}_v^* = \bar{T} \times k_d^0 = 0.105 \pm 0.050$ *versus* 0.047 ± 0.016 for $W \approx 1$ *versus* $W \approx 0.125$, respectively. Such defects are hypothesized as the cause of mechanical failure in associative networks such as vitrimers.[55] Indeed a decline in stress (as opposed to steady-state creep) is observed in cases where large voids develop. Thus, to ensure that force-dependent bond detachment alone, and not softening due to void nucleation, is responsible for the average observed induction of creep, cases in which voids formed are excluded in the computation of steady state stress reported in Fig. 8D. Furthermore, additional factors such as the goodness of solvent may significantly impact the onset of damage and consequently the global stress response in real materials such as gels.[56] Therefore, these factors should be considered on a material-specific basis for in-depth studies of damage. Nevertheless, these preliminary results generally suggests that damage in rate dependent transient networks is exacerbated by increased loading rate. Additionally, the emergence of voids represents a consequence of mesoscopic heterogeneity that influences global mechanical response, yet which the continuum model cannot predict: weakening due to nucleation of defects that are too large to heal on the timescale of individual bond exchanges. As such, further investigations of damage in transient networks may be conducted *via* this model in forthcoming work.

4.2 Effects of chain concentration

Having observed the effects of strain rate on the network response, we now turn to explore the effects of chain concentration at low strain rates. For this, we sweep the number of tethers per node, $n \in [2, 4, 10]$, which produces measured chain concentrations of $c \approx 15\zeta^{-2}$ ($Z \approx 8.4$), $c \approx 6.5\zeta^{-2}$ ($Z \approx 3.6$), and $c \approx 3.3\zeta^{-2}$ ($Z = 1.8$), respectively, while deforming the domain at a relatively low strain rate of $W \approx 1/6$.

4.2.1 Low chain concentration leads to over-predicted network stress by the continuum approach. We confirm that at high concentrations the continuum model predicts the stress response of the discrete model fairly well throughout the deformation history, barring the discrepancies discussed in Section 4.1. However, at lower concentrations, when $c \leq 6.5\zeta^{-2}$ ($Z \approx 3.8$), the TNT overestimates the stress response (Fig. 9A). Observing the probability joint distribution functions of r (Fig. 9B and C), it is clear that at low concentrations, chains tend to occupy the shorter (*i.e.*, lower energy) configurations available to them more readily. Therefore, it is unsurprising
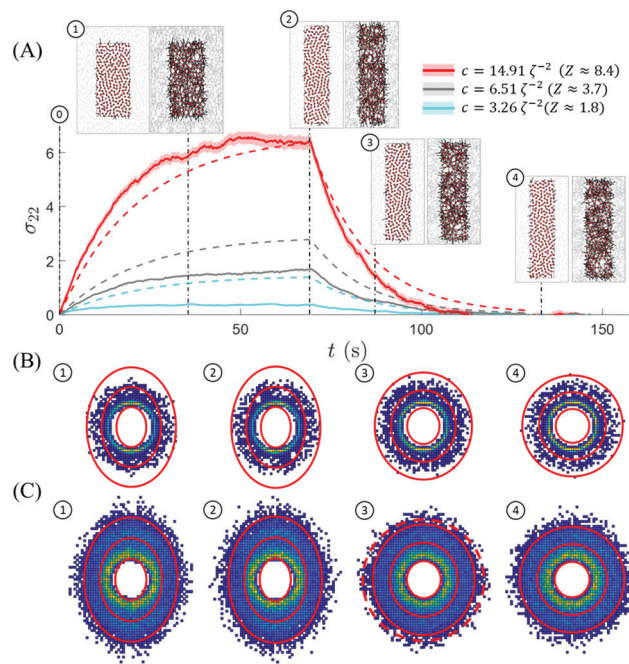

Fig. 9 (A) The stress response for the full loading history of Fig. 6A is plotted with respect to time for $Z \approx 1.8$ (cyan), $Z \approx 3.6$ (grey), and $Z \approx 8.4$ (red), respectively. Solid curves with shaded regions represent discrete data with standard error, while dotted curves represent the stress response predicted by TNT. The inset depictions of the networks at each time visually illustrate how n influences the network topology through chain concentration. Insets on the left always depict networks for which $n = 2$, while insets on the right depict networks with $n = 10$. (B and C) The ensemble joint distributions of r from ten numerical experiments are displayed as 2D histograms for (B) $n = 2$ and (C) $n = 10$. r, as predicted by $r = \mu r_0$, is plotted as red ellipses for initial end-to-end lengths of $|r_0| = [0.5, 1, 1.5]$.

that the networks stress is reduced for domains with fewer chains. That chains occupy these lower energy states to begin with is driven by the distance-dependent rates of k_a and k_d discussed in Section 3, which ensure that higher fractions of chains will occupy lower end-to-end distance configurations (Fig. 4B). Yet, another possible softening effect is that units in networks with lower connectivity have higher conformational degrees of freedom and may deform non-affinely, as needed, to a lower energy state than that predicted by TNT (which assumes instantaneously affine chain evolution $\dot{r} = Lr$).

4.2.2 Both bond kinetics and conformational changes contribute to non-affine deformation within a finite time interval. As discussed above, the continuum model relies on the instantaneously affine assumption that the rate change of a chain's end-to-end vector evolves according to $\dot{r} = Lr$ where L is the globally applied velocity gradient. To approximately test this in the discrete model, we quantified the extent of non-affine network deformation according to:

$$\delta u^* = \left\langle \frac{\|\delta u\|}{\|u_{\text{aff}}\|} \right\rangle, \tag{21}$$

where $\langle\rangle$ denotes taking the ensemble average over all $N^{\alpha\beta}$ chains that remain attached during the time interval from t to

$t + \tau$, $\delta \boldsymbol{u} = \boldsymbol{r}^{\alpha\beta}(t + \tau) - \boldsymbol{r}_{\text{aff}}^{\alpha\beta}(t + \tau)$, and $\boldsymbol{u}_{\text{aff}} = \boldsymbol{r}_{\text{aff}}^{\alpha\beta}(t + \tau) - \boldsymbol{r}^{\alpha\beta}(t)$.[57] Here, $\boldsymbol{r}^{\alpha\beta}$ and $\boldsymbol{r}_{\text{aff}}^{\alpha\beta}$ represent the actual and affinely predicted chain end-to-end vectors, respectively, at time $t + \tau$. The latter, $\boldsymbol{r}_{\text{aff}}^{\alpha\beta}$, is calculated according to:

$$\boldsymbol{r}_{\text{aff}}^{\alpha\beta}(t + \tau) = \boldsymbol{F}_\tau \boldsymbol{r}^{\alpha\beta}(t), \tag{22}$$

where $\boldsymbol{F}_\tau$ is the globally applied deformation gradient from time t to $t + \tau$. By definition, $\delta u^\star = 0$ when the network deformation is affine and $\delta u^\star \to 0$ in the limit $\tau \to 0$.

In this framework, network connectivity is modulated through the total number of tethers as opposed to by changing the bonds' attachment or detachment rates. As such, a network with more tethers will have more total bond reactions per unit volume within a given time interval and undergo a greater degree of configurational change. Therefore, to isolate the degree of non-affine deformation due to conformational effects (*e.g.*, floppy modes[24]), as opposed to network restructuring, we normalize $\delta u^\star$ by the total number of network tethers $\mathcal{N}n$, which scales proportionally to the density of bond reactions. Indeed, observing Fig. 10, we see that non-affine deformation due to conformational change increases in time, but is negligible in the limit $\tau \to 0$, which is consistent with the instantaneously affine assumption. We also see that non-affine deformation is amplified for networks with lower connectivities. Since non-affine deformation modes allow networks to reduce their free energy (thus softening their mechanical responses),[19,24] this is the likely explanation for the underestimation of network stress by the continuum model at low chain concentrations. In the remainder of this work, we examine a modification to the continuum approach (through the phantom network theory[24,58]) that is meant to correct for non-affine softening effects.

4.2.3 Correction to network stiffness through phantom network theory leads to under-prediction of the network stress by the continuum approach.

Through the conventional TNT, a network's shear modulus is taken as $G = ck_{\text{b}}T$. However, to adjust for non-affine effects the phantom network theory poses a correction to the instantaneous shear modulus as follows:[24]

$$G = \left(1 - \frac{2}{Z}\right)ckT, \tag{23}$$

for $Z \geq 2$ and $G = 0$ for $Z < 2$. The shear modulus of discrete networks is estimated according to the relation $G = 2E(1 + \nu)$,
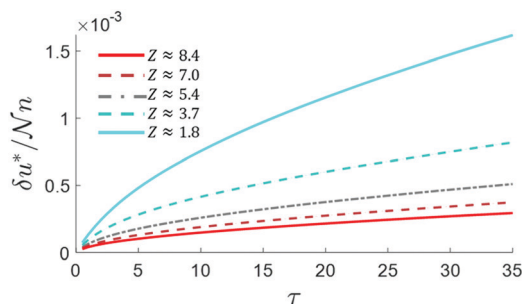

Fig. 10 (A) $\delta \boldsymbol{u}^\star / \mathcal{N}n$ is plotted with respect to time interval, τ, for networks in which $\bar{Z} \approx 1.8$ (solid cyan), $\bar{Z} \approx 3.7$ (dashed teal), $\bar{Z} \approx 5.4$ (dotted-dashed grey), $\bar{Z} \approx 7.0$ (dashed maroon), and $\bar{Z} \approx 8.4$ (solid red).

where E is the Young's modulus, and ν is the Poisson's ratio ($\nu = 0.5$, given enforced incompressibility). For each network connectivity, E is taken as the initial tangent modulus of the stress–strain response ($E \approx \partial\sigma/\partial\varepsilon$), based on the assumption that dissipative effects of networks near their stress-free configurations and over short timescales are negligible. This assumption is valid given that the networks begin at roughly stress-free states and the time interval over which E is measured ($\sim\Delta t$) is much smaller than the timescale of bond dynamics ($\bar{k}_{\text{d}}^{-1}$). Indeed, examining Fig. 11A we see that this correction introduces good agreement between the shear modulus predicted by the TNT and discrete models. Nevertheless, as displayed in Fig. 11B, applying this correction to the TNT leads to the ubiquitous under-prediction of network stress by the continuum approach due to use of Langevin chains in the discrete model. Furthermore, a finite modulus remains measurable for discrete networks even below the percolation threshold of $Z = 2$.

4.2.4 A small tensile stress can exist below the percolation threshold.

The correction from the phantom network theory dictates that no network stress will exist for networks below the percolation threshold of $Z = 2$. However, as displayed in Fig. 11A, the discrete model indicates that a finite tensile stress remains present even when $Z < 1$ (or $n = 1$). In such cases the measured stress cannot be the result of percolation, rather it is due to the alignment of disconnected chains. To better understand this effect, we revisit the computation of virial stress through eqn (18). Recalling that pairwise volume exclusion forces occur between all neighboring units, we recognize that this produces a roughly isotropic contribution to the stress. As such, any preferential alignment of the chains, which can only carry tension, culminates in a finite normal stress that is not balanced by the isotropic volume exclusion. To quantitatively gauge chain alignment, we computed the ensemble average metric tensor of $\boldsymbol{r}$, $\boldsymbol{g}$, defined as:

$$g_{ij} = \frac{1}{Vc_{\text{t}}} \sum_\alpha^{\mathcal{N}} \sum_\beta r_i^{\alpha\beta} \otimes r_j^{\alpha\beta}. \tag{24}$$

The diagonal components of $\boldsymbol{g}$ indicate the degree to which chains are aligned with the components of the orthonormal basis $\{\boldsymbol{e}_1, \boldsymbol{e}_2\}$, where $g_{11} > g_{22}$ indicates that chains are more aligned with $\boldsymbol{e}_1$ than $\boldsymbol{e}_2$, and $g_{11} \approx g_{22}$ indicates no preferential alignment. Examining g_{11} and g_{22} in Fig. 11C and D, it is clear that even when the networks are below the percolation threshold ($Z < 2$), the chains align with the direction of applied extension (*i.e.*, g_{22} increases during loading, while g_{11} decreases). Chain alignment is the origin of measurable stress for networks below the percolation threshold in this model, and is perhaps comparable to the stress evolution which occurs in dilute solutions of dumbbell-like polymers (*e.g.*, dimers or finitely-extensible nonlinear elastic polymers) or viscoelastic fluids undergoing shear flows.[59,60] However, unlike these dilute systems, the discrete model is representing compactly confined nodes. Furthermore, the current iteration does not capture the solute–solvent interactions which are often critical to the hydrodynamic effects of such systems.[59,61] Therefore, while
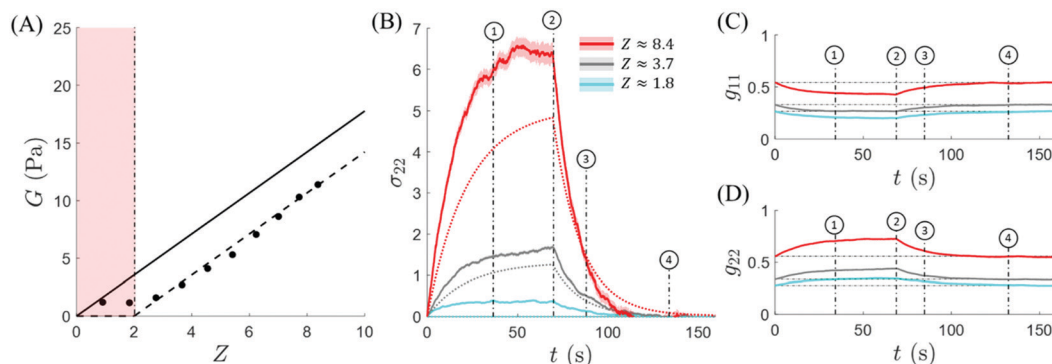
Fig. 11 (A) The network stiffness, G, is plotted with respect to Z for the numerical model as discrete data, and the continuum theory as a continuous black curve for the unadjusted model ($G = ckT$) and a dashed black curve for the adjusted model ($G = (1 - 2/Z)ckT$). The region shaded in red represents the non-percolated regime in which the adjusted TNT predicts no finite modulus. (B) The stress response predicted by the discrete model (continuous curves with shaded regions to represent standard error) and TNT (dashed curves) corrected through eqn (23), are plotted with respect to time. (C and D) The normal components of $\boldsymbol{g}$ in direction (C) $\boldsymbol{e}_1$ and (D) $\boldsymbol{e}_2$ are plotted with respect to time. (B–D) Results from networks with average connectivities of $Z \approx 1.8$ (cyan), $Z \approx 3.6$ (grey), and $Z \approx 8.4$ (red) are provided.

commenting on the effects observed below the percolation threshold, here we primarily focused on the findings of these models in the regime $Z > 2$.

5 Summary and concluding remarks

Ultimately, we have introduced a coarse-grained, discrete numerical model that allows us to directly investigate topological changes in transient networks without the high computational cost stemming from modeling the elemental constituents. To better represent the set of networks that can be examined through this model, we incorporated nonlinear Langevin chains,[46] probabilistic slip-bond detachment through Eyring's[21] or Bell's[28] model, and probabilistic bond reattachment based on Rouse diffusion of tethered chains,[38] thereby capturing the energetic penalty associated with highly stretched networks. Despite these features, we find that the idealized TNT approach,[9] which assumes linear chains and constant bond dynamics, provides excellent agreement with the numerical model when low strain rates are applied and network connectivity is high. Therefore, this discrete method may be feasibly incorporated into a quasicontinuum[32–34] framework in which regions exhibiting low stretch and heterogeneity are efficiently modeled through the TNT,[16] while regions of high local stretch, such as those near crack tips or other stress concentrations, are modeled through the newly introduced approach. While quasicontinuum models have recently been developed for irregular networked materials undergoing rate-dependent, permanent damage[33,34] to our knowledge no framework has been developed for fully dynamic, self-healing networks. Yet, as recently discussed by Ghareeb and Elbanna (2021),[34] quasicontinuum modeling also lends itself to comparable investigation in such materials. This model constitutes one possible discrete modelling component of such an approach for networks with fully reversible bond dissociation.

Whether a quasicontinuum or purely discrete framework is used, our results suggests that network discretization remains crucial in regions of high stretch for a couple of reasons. First, the finite length of true entropic chains (here captured using the Langevin chain model) consistently serves to stiffen the network and its effects become significant when the rate of deformation exceeds that of relaxation. Second, we find that force-dependent bond dynamics induce steady state creep in the discrete model, at high strain rates for which elastic behavior is predicted by the TNT. This same force-dependent bond detachment also induces non-exponential stress decay. Indeed, the numerical approach appears to capture two key features that the continuum model does not: variability of bond kinetics and heterogenization of network topology. Despite variability in the detachment rate, the discrete model predicts conservation of overall mean network connectivity, indicating that the networks, while not enforceably or locally associative, behave macroscopically as such. One might expect that conservation of connectivity precludes the loss of mechanical strength; yet, the discrete model also predicts the occasional nucleation of voids whose dimensions are too large for chains to reattach across. The formation of such voids induces loss of mechanical strength and it is believed that void nucleation likely precedes the onset of fracture or "damage" in dynamic networks despite the reversibility of their bonds.[55]

5.1 Limitations of the discrete model

A number of simplifications exist in the current numerical framework that limit the generality of this approach. Firstly, we assume monosdispersity in chain lengths; however, given polydispersity's effects on network mechanics,[47] it may be included in future work. Regarding the force–extension of single chains, we include no enthalpic bending contribution and the cross-links are modeled as freely attached pin joints,[24] limiting this current iteration of the model to networks of flexible chains. Since no energetic penalty is incurred for bending, chains can attach with equi-probability in any direction. Therefore, to mitigate directional biases in attachment between nearest neighbors and facilitate homogenization of

network topology, neighboring units are not permitted to attach more than once. However, this simplification is not intrinsically gotten from the underlying physics. Finally, the effects of solvent–solute interactions are neglected, which suspends considerations such as depletion[62] or drag forces[61] from the current framework. Although these limitations do not impact the findings of this work, they must be addressed for the study of specific considerations in future work.

For the extension of this model to damage and self-healing, several limitations must be addressed. Firstly, here network incompressibility is enforced through the condition $\det(\boldsymbol{F}) = 1$ rather than being an outcome of the underlying physical interaction potentials between nodes. In future work, compressible uniaxial tension with traction free bounds may be conducted on networks whose Poisson's ratio is dictated by their inter-unit potentials. Given some attractive regime (*e.g.*, that of Lennard-Jones potentials[63]), these interactive potentials will introduce an effective surface tension that governs compressibility (or the lack thereof). Secondly, irreversible damage of chains that are overly stretched is omitted from the current framework, but is needed for the prospective study of permanent damage,[29,30,64] which can impact the number of available chains for reattachment. Lastly, the positions of individual stickers are not tracked in the current framework. Although this does not impact detachment kinetics, it may influence the timescale and bias the direction of reattachment once hetereogeneities in the distribution of nodes (*i.e.*, through damage) develop. Tracking the diffusion-driven positions of free stickers in a manner that more directly reflects the work of Stukalin *et al.* (2013)[38] would mitigate these concerns and also eliminate the need for restrictive simplifications such as the prohibition of double connections between neighboring nodes.

5.2 Future work

In future work, we aim to explore a number of additional considerations that restrict the application of continuum theory, including the effects of compressible deformation and its influence on phenomena such as void nucleation (or cavitation), and void coalescence.[7,65] Cavitation, especially in regions of highly localized stress (*e.g.*, ahead of crack tips),[66] has been observed as the cause of mechanical failure of soft materials loaded under not only hydrostatic, but also uniaxial tension.[67] Yet, much remains uncertain about when cavities form, how they grow (or coalesce), and how this leads to mechanical failure. More importantly, it remains unclear how the evolution of damage phenomena relates to the underlying chain properties of networks. Availability of experimental data for such considerations remains sparse.[67] However, in forthcoming work the discrete model introduced here will allow us to explore these features through controlled, *in silico* experimentation. Specifically, this model will permit direct observation of the damage zone near a crack tip, wherein both damage and viscoelastic deformation contribute to energy dissipation and failure onset. Such detailed exploration could elucidate the size of the damage zone and nature of the

dissipative mechanisms, thereby revealing the intrinsic fracture toughness of the network.

Author contributions

Robert J. Wagner: conceptualization, methodology, software, data curation, investigation, formal analysis, validation, writing-original draft, visualization. Ethan Hobbs: methodology, software, data curation, investigation, formal analysis, validation. Franck J. Vernerey: conceptualization, methodology, funding acquisition, resources, supervision, writing-original draft.

Conflicts of interest

There are no conflicts to declare.

Acknowledgements

Notes and references

1 H. Tabuteau, S. Mora, G. Porte, M. Abkarian and C. Ligoure, *Phys. Rev. Lett.*, 2009, **102**, 155501.
2 S. Fürthauer, B. Lemma, P. J. Foster, S. C. Ems-McClung, C.-H. Yu, C. E. Walczak, Z. Dogic, D. J. Needleman and M. J. Shelley, *Nat. Phys.*, 2019, **15**, 1295–1300.
3 M. Tennenbaum, Z. Liu, D. Hu and A. Fernandez-Nieves, *Nat. Mater.*, 2016, **15**, 54–59.
4 F. J. Vernerey, T. Shen, S. L. Sridhar and R. J. Wagner, *J. R. Soc., Interface*, 2018, **15**, 20180642.
5 O. Peleg, J. M. Peters, M. K. Salcedo and L. Mahadevan, *Nat. Phys.*, 2018, **14**, 1193–1198.
6 F. J. Vernerey, R. Brighenti, R. Long and T. Shen, *Macromolecules*, 2018, **51**, 6609–6622.
7 T. Shen and F. J. Vernerey, *J. Mech. Phys. Solids*, 2020, **143**, 104028.
8 N. Roy, B. Bruchmann and J.-M. Lehn, *Chem. Soc. Rev.*, 2015, **44**, 3786–3807.
9 F. J. Vernerey, R. Long and R. Brighenti, *J. Mech. Phys. Solids*, 2017, **107**, 1–20.
10 S. A. Rincon, A. Lamson, R. Blackwell, V. Syrovatkina, V. Fraisier, A. Paoletti, M. D. Betterton and P. T. Tran, *Nat. Commun.*, 2017, **8**, 15286.
11 C. Shi, Z. Zou, Z. Lei, X. Wu, Z. Liu, H. Lu, W. Zhang and J. Xiao, *J. Appl. Mech.*, 2019, **86**, 101005.
12 S. Lalitha Sridhar, J. Dunagin, K. Koo, L. Hough and F. Vernerey, *Macromolecules*, 2021, **54**, 1850–1858.
13 A. Gooneie, S. Schuschnigg and C. Holzer, *Polymers*, 2017, **9**, 16.
14 T. Koga and F. Tanaka, *Eur. Phys. J. E: Soft Matter Biol. Phys.*, 2005, **17**, 115–118.
15 C.-Y. Hui and R. Long, *Soft Matter*, 2012, **8**, 8209–8216.

16 T. Shen, R. Long and F. Vernerey, *Comput. Mech.*, 2019, **63**, 725–745.

17 Y. Yu, N. Bouklas, C. M. Landis and R. Huang, *J. Appl. Mech.*, 2018, **85**, 111011.

18 P. L. Chandran and V. H. Barocas, *J. Biomech. Eng.*, 2005, **128**, 259–270.

19 Q. Wen, A. Basu, P. A. Janmey and A. G. Yodh, *Soft Matter*, 2012, **8**, 8039–8049.

20 R. Petrosyan, *Rheol. Acta*, 2017, **56**, 21–26.

21 H. Eyring, *Chem. Rev.*, 1935, **17**, 65–77.

22 A. P. Tabatabai, D. S. Seara, J. Tibbs, V. Yadav, I. Linsmeier and M. P. Murrell, *Adv. Funct. Mater.*, 2021, **31**, 2006745.

23 A. Aksimentiev and R. Hołyst, *Progr. Polym. Sci.*, 1999, **24**, 1045–1093.

24 R. C. Picu, *Soft Matter*, 2011, **7**, 6768.

25 H. Hatami-Marbini and R. C. Picu, *Physical Review E*, 2008, **77**, 062103.

26 H. Hatami-Marbini and M. Rohanifar, *Soft Matter*, 2020, **16**, 7156–7164.

27 S. Arbabi and M. Sahimi, *Physical Review B*, 1993, **47**, 695–702.

28 G. I. Bell, *Science*, 1978, **200**, 618–627.

29 A. E. Elbanna and J. M. Carlson, *PLoS One*, 2013, **8**, e56118.

30 K. Kothari, Y. Hu, S. Gupta and A. Elbanna, *J. Appl. Mech.*, 2018, **85**, 031008.

31 L. A. A. Beex, P. Kerfriden, T. Rabczuk and S. P. A. Bordas, *Comput. Methods Appl. Mech. Eng.*, 2014, **279**, 348–378.

32 K. Mikeš and M. Jirásek, *Comput. Struct.*, 2017, **192**, 50–70.

33 A. Ghareeb and A. Elbanna, *J. Mech. Phys. Solids*, 2020, **137**, 103819.

34 A. Ghareeb and A. Elbanna, *J. Appl. Mech.*, 2021, 1–22.

35 Z. Yang, Q. Wang and T. Wang, *ACS Appl. Mater. Interfaces*, 2016, **8**, 21691–21699.

36 Z. Song, Z. Wang and S. Cai, *Mech. Mater.*, 2021, **153**, 103687.

37 G. Singh and V. Sundararaghavan, *Chem. Phys. Lett.*, 2020, **760**, 137966.

38 E. B. Stukalin, L.-H. Cai, N. A. Kumar, L. Leibler and M. Rubinstein, *Macromolecules*, 2013, **46**, 7525–7541.

39 S. Tang, A. Habicht, S. Li, S. Seiffert and B. D. Olsen, *Macromolecules*, 2016, **49**, 5599–5608.

40 Y. Li, L. Yang, Y. Zeng, Y. Wu, Y. Wei and L. Tao, *Chem. Mater.*, 2019, **31**, 5576–5583.

41 F. J. Vernerey, *J. Mech. Phys. Solids*, 2018, **115**, 230–247.

42 N. P. Thien and R. I. Tanner, *J. Non-Newtonian Fluid Mech.*, 1977, **2**, 353–365.

43 M. Doi and S. F. Edwards, *J. Chem. Soc., Faraday Trans. 2*, 1979, 38–54.

44 S. Q. Wang, *Macromolecules*, 1992, **25**, 7003–7010.

45 F. Tanaka and S. F. Edwards, *Macromolecules*, 1992, **25**, 1516–1523.

46 A. Cohen, *Rheol. Acta*, 1991, **30**, 270–273.

47 B. Li and N. Bouklas, *Int. J. Solids Struct.*, 2020, **182–183**, 193–204.

48 Y. Mao, B. Talamini and L. Anand, *Extreme Mech. Lett.*, 2017, **13**, 17–24.

49 S. Ahmadi, M. Schmidt, R. J. Spiteri and R. K. Bowles, *J. Chem. Phys.*, 2019, **150**, 224501.

50 C. K. C. Lieou, A. E. Elbanna and J. M. Carlson, *Physical Review E*, 2013, **88**, 012703.

51 G. E. Fantner, T. Hassenkam, J. H. Kindt, J. C. Weaver, H. Birkedal, L. Pechenik, J. A. Cutroni, G. A. G. Cidade, G. D. Stucky, D. E. Morse and P. K. Hansma, *Nat. Mater.*, 2005, **4**, 612–616.

52 J. Adams, G. E. Fantner, L. W. Fisher and P. K. Hansma, *Nanotechnology*, 2008, **19**, 384008.

53 J. C. Meza, *Wiley Interdiscip. Rev.: Comput. Mol. Sci.*, 2010, **2**, 719–722.

54 A. K. Subramaniyan and C. T. Sun, *Int. J. Solids Struct.*, 2008, **45**, 4340–4346.

55 Z. Song, T. Shen, F. J. Vernerey and S. Cai, arXiv:2105.02775 [cond-mat], 2021.

56 S. Kundu and A. J. Crosby, *Soft Matter*, 2009, **5**, 3963–3968.

57 P. R. Onck, T. Koeman, T. van Dillen and E. van der Giessen, *Phys. Rev. Lett.*, 2005, **95**, 178102.

58 T.-S. Lin, R. Wang, J. A. Johnson and B. D. Olsen, *Macromolecules*, 2019, **52**, 1685–1694.

59 P. S. Doyle, E. S. G. Shaqfeh, G. H. McKinley and S. H. Spiegelberg, *J. Non-Newtonian Fluid Mech.*, 1998, **76**, 79–110.

60 D. Won and C. Kim, *J. Non-Newtonian Fluid Mech.*, 2004, **117**, 141–146.

61 Q. Du, C. Liu and P. Yu, *Multiscale Model. Simul.*, 2005, **4**, 709–731.

62 S. A. Egorov, *Physical Review E*, 2004, **70**, 031402.

63 K. Koura and H. Matsumoto, *Phys. Fluids A*, 1991, **3**, 2459–2465.

64 C. Nguyen, D. Peetz, A. E. Elbanna and J. M. Carlson, *Physical Review E*, 2019, **100**, 042402.

65 Z. Song and S. Cai, *Acta Mech. Sin.*, 2021, **37**, 767–772.

66 J. Guo, A. T. Zehnder, C. Creton and C.-Y. Hui, *Soft Matter*, 2020, **16**, 6163–6179.

67 C. Creton and M. Ciccotti, *Rep. Prog. Phys.*, 2016, **79**, 046601.